This article has been accepted for publication in a future issue of this journal, but has not been fully edited. Content may change prior to final publication. Citation information: DOI 10.1109/OJAP.2021.3057060, IEEE Open Journal of Antennas and Propagation

Microwave Tomography with LSTM-Based Processing of the Scattered Field

Alessandro Fedeli, *Member, IEEE*

Abstract The quantitative inspection of unknown targets or bodies by means of microwave tomography requires a proper modeling of the field scattered by the structures under test, which in turn depends on several factors related to the adopted antennas and measurement configuration. In this paper, a multifrequency tomographic approach in nonconstant-exponent Lebesgue spaces is enhanced by a preliminary step that processes the measured scattered field with a neural network based on long short-term memory cells. In the considered cases, this approach allows dealing with measurements in three-dimensional settings obtained with non-ideal antennas and measurement points, while retaining a canonical two-dimensional formulation of the inverse problem. The adopted data-driven model is trained with a set of simulations of cylindrical targets performed with a finite-difference time domain method, considering a simplified bistatic measurement configuration as an initial case study. The inversion procedure is then validated with numerical simulations involving cylindrical and spherical structures.

***Index Terms*—Microwave imaging, inverse scattering, long short-term memory.**

I. Introduction

THE RECENT advances in microwave imaging are paving the way to many interesting scenarios, which range from innovative biomedical diagnostics [1], [2] to security applications [3], [4] and civil engineering [5].

The attractive possibility of analyzing unknown targets and bodies by means of microwave radiation has stimulated the research community for decades and is nowadays at a turning point [6], [7]. On the one hand, the development of advanced inverse scattering techniques is demonstrating the ability to deal with complex scenarios [8]–[12], which is supported by the design of proper antennas [13]–[17] and measurement systems [18]–[20]. On the other hand, the ever-increasing available computing power is providing unvaluable tools for the practical implementation of the proposed solution techniques. In this rapidly-evolving situation, the recent introduction of novel methods based on artificial intelligence [21] and in particular deep learning approaches [22], [23] is opening new doors, overcoming several limitations of the traditional inversion techniques and lowering computational times [24]–[27].

In the framework of quantitative microwave tomography, an interesting class is represented by nonlinear Newton-based approaches [28]–[30], which have also been recently formulated in non-Hilbertian Lebesgue spaces with constant and nonconstant exponents [31]. The good performance of these methods has been proven in different case studies, with both single- and multifrequency data [32]. So far, this kind of tomographic Newton-based techniques have been formulated by considering excitations from infinite line-current sources and ideal observation domains [31], [33] or with rectangular waveguide models of the radiating and receiving antenna elements [34]. However, there are several situations where the assumption of idealized or simplified probing elements does not lead to correct results. Since the adopted antenna elements and measurement configurations have a significant impact on the measured scattered field – especially in near-field conditions – it is recommended to model or calibrate them within the inversion procedure.

One possible solution is to include advanced three-dimensional (3D) forward solvers with accurate numerical models of the antennas inside the inversion algorithm. However, this solution leads to a great increase in the required computational resources compared to a standard tomographic inversion with ideal sources and measurement points. In addition, a change in the probing elements may require substantial modifications in the solving procedure.

Another possibility, commonly practiced in microwave tomography, is data calibration in the frequency domain [35], [36]. This is usually done by considering the incident field or the field scattered by a known target [37]. In both cases, a set of complex coefficients are found to scale the measured quantities in order to match the field values simulated with the same numerical solver adopted for inversion. Among these methods, scattered field calibration is proven to be the most successful [30], [38]. It is worth noting that calibration techniques where antenna effects are modeled with characteristic coefficient functions [39], [40] or with radial basis functions networks [41] have also been

Manuscript submitted December 28, 2020; revised January 30, 2021; accepted February 1, 2021.

The Author is with the Department of Electrical, Electronic, Telecommunications Engineering and Naval Architecture (DITEN), University of Genoa, 16145 Genoa, Italy (e-mail: alessandro.fedeli@unige.it).

This article has been accepted for publication in a future issue of this journal, but has not been fully edited. Content may change prior to final publication. Citation information: DOI 10.1109/OJAP.2021.3057060, IEEE Open Journal of Antennas and Propagation

proven effective in monostatic and bistatic configurations.

In this paper, a different strategy is pursued: a time-domain data-driven processing of the scattered field is done, and the combination of this approach with a multifrequency tomographic method in nonconstant-exponent Lebesgue spaces is explored. In particular, the inversion method is enhanced by a preliminary step that processes the measured scattered field with a neural network based on long short-term memory (LSTM) cells [42]. The use of an LSTM-based network was selected in order to address the problem at hand in the time domain, which may be useful to process wideband data. Specifically, for sequence-to-sequence processing of time series, recurrent neural networks (RNNs) have shown advantages against standard convolutional neural networks (CNNs), e.g., the natural ability to process input sequences of arbitrary length without impacting on the network layout and size. Among RNN architectures, LSTMs are one of the most promising choices, as their ability to "selectively remember" their state allows them to capture long- and short-term dependencies between the input sequences of data in a very effective way, avoiding the tricky problem of vanishing gradients [43]. Due to these advantages, LSTMs are widely used in different areas (e.g., natural language processing) [44]. These interesting properties have also been successfully exploited to predict the evolution of field values in transient electrodynamics [45] and for buried object detection from ground penetrating radar signals [46].

In our case, the LSTM-based network is trained to learn the connection between the time-domain scattered field measured by non-ideal probing elements in the 3D case (assuming a cylindrical configuration) and the corresponding scattered field that would be given by a canonical two-dimensional (2D) case with line-current sources and ideal measurement points. As a result, in the considered cases, this approach allows dealing with data collected in 3D cylindrical configurations with non-ideal probes, while retaining a canonical 2D formulation of the inverse problem. Of course, this connection is intrinsically approximate, but leads to significant benefits in the quantitative reconstruction of unknown scatterers. It is interesting to notice that such an approach shares the same goal of the scattered field calibration techniques, although the problem is tackled from a different perspective.

The adopted model is trained with a set of simulations performed with a finite-difference time domain (FDTD) solver, and the inversion approach is then initially validated with numerical simulations. As a first case study, a bistatic measurement configuration has been considered, since it allows speeding up the model training and checking the behavior of LSTM-based processing in a precise and rather simple way, by analyzing B-scan-like images. Moreover, the bistatic case models a quite challenging configuration for the quantitative inversion (that can be found, for example, in through-the-wall or ground penetrating radar

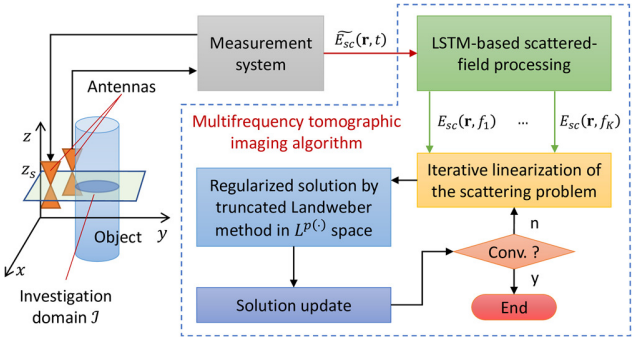

Fig. 1. Configuration of the imaging problem and proposed approach to microwave tomography.

configurations) where small errors may impair a correct reconstruction of targets. Therefore, it represents a case where a correct modeling of the scattered field is essential.

The paper has the following organization. Section II formulates the inverse problem, discussing both the preprocessing step and the imaging scheme. Results achieved in a simulated environment are reported in Section III. Finally, Section IV delineates concluding remarks.

II. Problem Formulation and Inversion Scheme

The configuration of the imaging problem and the proposed inversion approach are drafted in Fig. 1. We assume to scan an object under test, characterized by an unknown dielectric permittivity $\epsilon(\mathbf{r})$ and electric conductivity $\sigma(\mathbf{r})$, by means of set of antennas (e.g., two elements). The goal is to reconstruct the spatial distribution of the dielectric properties of the target in a cross-sectional investigation domain $\mathcal{I}$. Both antennas and $\mathcal{I}$ are aligned on the same horizontal plane at $z = z_s$. Antennas are connected to a time-domain measurement system, whose output is a quantity related to the z-component of the scattered electric field, $\widetilde{E_{sc}}(\mathbf{r},t)$. Here, $\mathbf{r}$ indicates the position of the receiving antenna element and t is the time.

In a near-field 3D configuration, the presence of the antenna structures may have a non-negligible influence on the measured scattered field. In other words, $\widetilde{E_{sc}}(\mathbf{r},t)$ not only depends on the target properties, but also on the characteristics of the measurement system and the deployed antennas, due to their direct interaction with the (unknown) object under test. Sometimes these effects can be neglected to some extent. Nevertheless, if such an interaction cannot be ignored, an adequate modeling of the measurement configuration inside the imaging algorithm is required to obtain a suitable quantitative reconstruction of the dielectric properties of the target. This work primarily aims at dealing with near-field conditions, and this makes different the framework of this contribution with respect to standard antenna and geometry compensation strategies.

Here we try to retain a 2D formulation of the inversion algorithm with a canonical tomographic measurement configuration characterized by ideal observation points and line-current sources. Of course, even in the presence of the

This article has been accepted for publication in a future issue of this journal, but has not been fully edited. Content may change prior to final publication. Citation information: DOI 10.1109/OJAP.2021.3057060, IEEE Open Journal of Antennas and Propagation

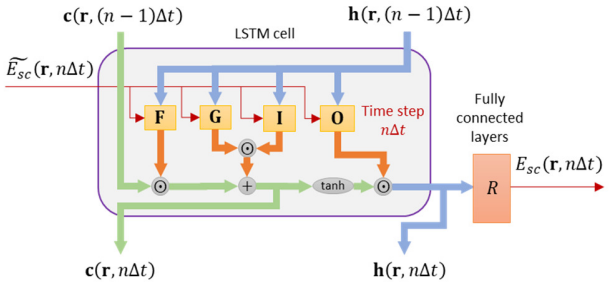

Fig. 2. Proposed LSTM-based processing of the scattered field at the time step $n\Delta t$: scheme of a single LSTM-FC block. Thick arrows denote vector quantities; scalar values are indicated by thin arrows.

same object under test, the scattered electric field expected by the inversion algorithm, $E_{sc}(\mathbf{r},t)$, would be different from $\widetilde{E_{sc}}(\mathbf{r},t)$. This modification in the scattered field is modeled by the LSTM-based approach described in Section II.A, whose objective is to estimate $E_{sc}(\mathbf{r},t)$ from the measured values. Subsequently, data are converted to the frequency domain and processed by a nonlinear multifrequency tomographic approach formulated in Lebesgue spaces $L^{p(\cdot)}$ with nonconstant exponent function, outlined in Section II.B.

A. *LSTM-based preprocessing of the scattered field*

For processing the scattered field input data to feed the microwave tomographic algorithm, we define a data-driven model that maps the measured scattered field $\widetilde{E_{sc}}$ to its counterpart E_{sc} given by a canonical measurement configuration. In other words, we aim at finding a nonlinear operator $\mathcal{N}$ such that

$$E_{sc}(\mathbf{r},t) = \mathcal{N}\left(\widetilde{E_{sc}}(\mathbf{r},t)\right). \tag{1}$$

Let us suppose that the scattered field $\widetilde{E_{sc}}(\mathbf{r},t)$ is known at the discrete time steps $n\Delta t$, with $n = 0,\dots,N$. For each time step, $\mathcal{N}$ is modeled with a neural network based on LSTM cells, whose output is processed by fully connected (FC) neural layers. The architecture of the adopted LSTM-FC cell is reported in Fig. 2.

At the nth time step, the LSTM cell receives in input the measured scattered field $\widetilde{E_{sc}}$ and two "state" vectors that allow remembering information about the previous time history of the scattered field component, namely the *cell state* $\mathbf{c} \in \mathbb{R}^S$ and the *hidden state* $\mathbf{h} \in \mathbb{R}^S$. These quantities are both real vectors of size S, and come directly from the previous time step, i.e., $(n-1)\Delta t$.

The first operation performed inside the LSTM is the decision about what to retain or forget from the previous cell state $\mathbf{c}(\mathbf{r},(n-1)\Delta t)$. This is done by the *forget gate* $\mathbf{F}$, whose vector output is given by

$$\begin{aligned}\mathbf{F}(\mathbf{r},n\Delta t) = \mathbf{S}\big(&\mathbf{W}_f\widetilde{E_{sc}}(\mathbf{r},n\Delta t)\\ &+\mathbf{R}_f\mathbf{h}(\mathbf{r},(n-1)\Delta t)+\mathbf{b}_f\big),\end{aligned} \tag{2}$$

where $\mathbf{W}_f \in \mathbb{R}^S$, $\mathbf{R}_f \in \mathbb{R}^{S\times S}$ and $\mathbf{b}_f \in \mathbb{R}^S$ are real parameters tuned by the training phase, and $\mathbf{S}(\cdot)$ denotes the sigmoid gate activation function. In particular, given a vector $\mathbf{x} = [x_1, x_2, \dots, x_S]^T$, we have

$$\mathbf{S}(\mathbf{x}) = \left[\frac{1}{1+e^{-x_1}}, \frac{1}{1+e^{-x_2}}, \dots, \frac{1}{1+e^{-x_S}}\right]^T. \tag{3}$$

Another important operation inside the LSTM is to define a possible *cell candidate*, i.e., a vector $\mathbf{G}$ that is used to update the cell state $\mathbf{c}$, computed as

$$\begin{aligned}\mathbf{G}(\mathbf{r},n\Delta t) = \mathbf{T}\big(&\mathbf{W}_g\widetilde{E_{sc}}(\mathbf{r},n\Delta t)\\ &+\mathbf{R}_g\mathbf{h}(\mathbf{r},(n-1)\Delta t)+\mathbf{b}_g\big),\end{aligned} \tag{4}$$

with $\mathbf{W}_g \in \mathbb{R}^S$, $\mathbf{R}_g \in \mathbb{R}^{S\times S}$, $\mathbf{b}_g \in \mathbb{R}^S$, and a state activation function

$$\mathbf{T}(\mathbf{x}) = [\tanh x_1, \tanh x_2, \dots, \tanh x_S]^T. \tag{5}$$

The update of the cell state is weighted by the so-called *input gate*

$$\begin{aligned}\mathbf{I}(\mathbf{r},n\Delta t) = \mathbf{S}\big(&\mathbf{W}_i\widetilde{E_{sc}}(\mathbf{r},n\Delta t)\\ &+\mathbf{R}_i\mathbf{h}(\mathbf{r},(n-1)\Delta t)+\mathbf{b}_i\big),\end{aligned} \tag{6}$$

where, like before, $\mathbf{W}_i \in \mathbb{R}^S$, $\mathbf{R}_i \in \mathbb{R}^{S\times S}$ and $\mathbf{b}_i \in \mathbb{R}^S$. Finally, the output of the LSTM cell is driven by the *output gate*, which is specified by the following function:

$$\begin{aligned}\mathbf{O}(\mathbf{r},n\Delta t) = \mathbf{S}\big(&\mathbf{W}_o\widetilde{E_{sc}}(\mathbf{r},n\Delta t)\\ &+\mathbf{R}_o\mathbf{h}(\mathbf{r},(n-1)\Delta t)+\mathbf{b}_o\big),\end{aligned} \tag{7}$$

with $\mathbf{W}_o \in \mathbb{R}^S$, $\mathbf{R}_o \in \mathbb{R}^{S\times S}$ and $\mathbf{b}_o \in \mathbb{R}^S$.

Having defined all these internal gates and their operation, the cell state at the time step $n\Delta t$ is computed as

$$\begin{aligned}\mathbf{c}(\mathbf{r},n\Delta t) = &\mathbf{F}(\mathbf{r},n\Delta t)\odot\mathbf{c}(\mathbf{r},(n-1)\Delta t)\\ &+\mathbf{I}(\mathbf{r},n\Delta t)\odot\mathbf{G}(\mathbf{r},n\Delta t),\end{aligned} \tag{8}$$

and the hidden state is calculated as

$$\mathbf{h}(\mathbf{r},n\Delta t) = \mathbf{O}(\mathbf{r},n\Delta t)\odot\mathbf{T}\big(\mathbf{c}(\mathbf{r},n\Delta t)\big), \tag{9}$$

where the operator $\odot$ represents an element-wise vector multiplication (Hadamard product).

The scattered field E_{sc} at time step $n\Delta t$ is then computed from the hidden state $\mathbf{h}(\mathbf{r},n\Delta t)$ by means of three fully connected layers; the first two layers have H neurons with hyperbolic tangent activation function, and the last one has a single neuron (scalar output), i.e.,

$$E_{sc}(\mathbf{r},n\Delta t) = R\big(\mathbf{h}(\mathbf{r},n\Delta t)\big) = \mathbf{W}_r^T\mathbf{R}_2(\mathbf{r},n\Delta t) + b_r \tag{10}$$

where $\mathbf{W}_r \in \mathbb{R}^H$, $b_r \in \mathbb{R}$,

$$\begin{aligned}\mathbf{R}_2(\mathbf{r},n\Delta t) = \mathbf{T}[&\mathbf{W}_{r12}^T\mathbf{R}_1(\mathbf{r},n\Delta t)+b_{r12},\dots,\\ &\mathbf{W}_{rH2}^T\mathbf{R}_1(\mathbf{r},n\Delta t)+b_{rH2}]^T\end{aligned} \tag{11}$$

$$\begin{aligned}\mathbf{R}_1(\mathbf{r},n\Delta t) = \mathbf{T}[&\mathbf{W}_{r11}^T\mathbf{h}(\mathbf{r},n\Delta t)+b_{r11},\dots,\\ &\mathbf{W}_{rH1}^T\mathbf{h}(\mathbf{r},n\Delta t)+b_{rH1}]^T\end{aligned} \tag{12}$$

with parameters $\mathbf{W}_{r11},\dots,\mathbf{W}_{rH1} \in \mathbb{R}^S$, $\mathbf{W}_{r12},\dots,\mathbf{W}_{rH2} \in \mathbb{R}^H$, $b_{r11},\dots,b_{rH1} \in \mathbb{R}$, $b_{r12},\dots,b_{rH2} \in \mathbb{R}$.

This article has been accepted for publication in a future issue of this journal, but has not been fully edited. Content may change prior to final publication. Citation information: DOI 10.1109/OJAP.2021.3057060, IEEE Open Journal of Antennas and Propagation

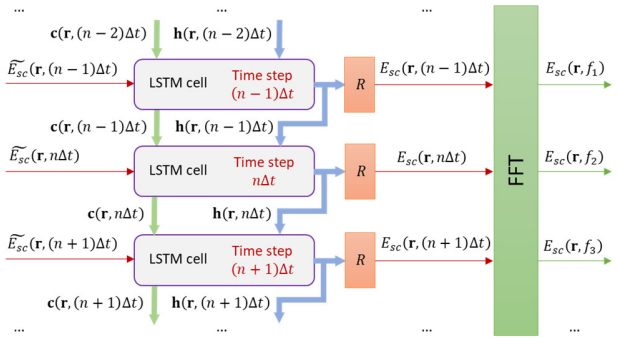

Fig. 3. Process diagram which described the extraction of frequency-domain data from time-domain scattered field measurements with the LSTM-FC network. As an example, three time steps have been unrolled.

As highlighted in Fig. 3, where three time steps are unrolled in order to understand the data processing workflow, the presence of the LSTM layer implies that $E_{sc}(\mathbf{r}, n\Delta t)$ is estimated by taking into account all the relevant information from the past evolution of the field component, which is remembered by the network by means of the state vectors **c** and **h.** After the scattered field at all the required time steps is processed, a fast Fourier transform (FFT) is applied to the resulting time series $E_{sc}(\mathbf{r}, n\Delta t)$, $n = 0, \dots, N$ in order to extract scattered field data at frequencies $f_1, \dots, f_K$. These data are directly given in input to the microwave tomographic algorithm outlined in the following section.

B. Tomographic inversion of scattered field data

The processed scattered field data are inverted in the frequency domain by assuming a scalar and two-dimensional EM model. We define a position vector $\mathbf{r}_t$ on the cross-sectional imaging plane such that $\mathbf{r} = \mathbf{r}_t + \hat{\mathbf{z}}z_s$. A multiview setup, with V positions of the source, is adopted for collecting scattered-field measurements. However, for the sake of simplicity, the single-view case is described here. For each view, the investigation domain is illuminated by a radiation generated by an ideal line-current source located at $\mathbf{r}_t^{TX}$ with a current density $\mathbf{J}_0(\mathbf{r}_t) = \hat{\mathbf{z}}I\delta(\mathbf{r}_t - \mathbf{r}_t^{TX})$. This source generates a transverse-magnetic incident radiation whose z-component of the electric field is $E_i(\mathbf{r}_t, f) = j2\pi f\mu_0 I g(\mathbf{r}_t|\mathbf{r}_t^{TX}, f)$, where f is the frequency, μ_0 is the magnetic permeability of vacuum, and $g(\mathbf{r}_t|\mathbf{r}_t^{TX}, f) = jH_0^{(2)}(k_0|\mathbf{r}_t - \mathbf{r}_t^{TX}|)/4$ is the related Green's function, with $k_0 = 2\pi f\sqrt{\mu_0\epsilon_0}$, ϵ_0 being the dielectric permittivity of vacuum. Under these hypotheses, if the object under test is infinite along the z axis, it causes a scattered field [7]

$$E_{sc}(\mathbf{r}_t, f) = -k_0^2 \int_{\mathcal{I}} g(\mathbf{r}_t|\mathbf{r}_t', f)\mathbf{H}(f)\mathbf{x}(\mathbf{r}_t')E_t(\mathbf{r}_t', f)d\mathbf{r}_t', \quad (13)$$

where the properties of the object are expressed with the term $\mathbf{x}(\mathbf{r}_t) = [(\epsilon(\mathbf{r}_t)/\epsilon_0 - 1) \quad \sigma(\mathbf{r}_t)/(2\pi f_1\epsilon_0)]^T$, $\mathbf{H}(f) = [1 \quad -jf_1/f]$, and $E_t(\mathbf{r}_t, f) = E_{sc}(\mathbf{r}_t, f) + E_i(\mathbf{r}_t, f)$ is the total electric field. Since E_t depends on $\mathbf{x}$, (13) reveals a nonlinear relationship between the scattered field and $\mathbf{x}$, which can be written as [31]

$$E_{sc}(\mathbf{r}_t, f) = \mathcal{F}_f(\mathbf{x})(\mathbf{r}_t). \quad (14)$$

For solving the inverse problem, the available values of the scattered electric field at K frequencies f_k $(k = 1, \dots, K)$ are simultaneously processed, forming a system of nonlinear equations:

$$\begin{bmatrix} E_{sc}(\mathbf{r}_t, f_1) \\ \vdots \\ E_{sc}(\mathbf{r}_t, f_K) \end{bmatrix} = \begin{bmatrix} \mathcal{F}_{f_1}(\mathbf{x})(\mathbf{r}_t) \\ \vdots \\ \mathcal{F}_{f_K}(\mathbf{x})(\mathbf{r}_t) \end{bmatrix}, \qquad \mathbf{r}_t \in \mathcal{O}, \quad (15)$$

where $\mathcal{O}$ is the observation domain where scattered-field data are collected by the measurement devices.

This system, which has to be solved in the unknown $\mathbf{x}$, can be compactly written as $\bar{E}_{sc} = \bar{\mathcal{F}}(\mathbf{x})$, with $\mathbf{x} \in A$, $\bar{E}_{sc} \in B$, and $\bar{\mathcal{F}}$ is a nonlinear operator such that $\bar{\mathcal{F}}: A \to B$. In the present approach, (15) is solved with an iterative strategy. At each iteration $i = 1, 2, \dots$ the nonlinear operator $\bar{\mathcal{F}}$ is subject to a Newton linearization around the current estimation of the unknown function $\mathbf{x}$, denoted as $\mathbf{x}_i$. Indicating with $\bar{\mathcal{F}}'_{\mathbf{x}_i}$ the Fréchet derivative of $\bar{\mathcal{F}}$ around $\mathbf{x}_i$, the resulting linearized counterpart of (15) is

$$\bar{E}_{sc} = \bar{\mathcal{F}}'_{\mathbf{x}_i}\boldsymbol{\delta}_i + \bar{\mathcal{F}}(\mathbf{x}_i) \quad (16)$$

The problem described by (16) is solved by the truncated Landweber technique in Lebesgue spaces $L^{p(\cdot)}$ with nonconstant exponents [47], where the space of unknown A is characterized by a variable exponent function $p_i(\mathbf{r}_t)$, $\mathbf{r}_t \in \mathcal{I}$, computed from the normalized magnitude of $\mathbf{x}_i$ as

$$p_i(\mathbf{r}_t) = 2 + \Delta p\left[\frac{\|\mathbf{x}_i(\mathbf{r})\|}{\max_{\mathbf{r}_t \in \mathcal{I}}\|\mathbf{x}_i(\mathbf{r})\|} - 1\right] \quad (17)$$

with Δp being the range of the exponent function. In the first Newton iteration a null starting guess $\mathbf{x}_1$ and a constant exponent $p_1(\mathbf{r}_t) = 2 - \Delta p$ are used. The application of (17) leads to low values of $p_i(\mathbf{r}_t)$ outside the detected targets, and higher values inside. As to the space of data B, a constant exponent equal to the average of $p_i(\mathbf{r}_t)$ in the investigation domain $\mathcal{I}$ is assumed. Once that $\boldsymbol{\delta}_i$ is found by solving (16), this term is applied to update the unknown as $\mathbf{x}_{i+1} = \mathbf{x}_i + \boldsymbol{\delta}_i$, and a new linearization/solution process is executed until convergence is reached.

III. Numerical Validation of the Approach

The approach to microwave tomography described in the previous sections has been validated by means of numerical simulations. In more detail, the validation consisted in two distinct phases. The first one, explained in Section III.A, is dedicated to the training of the model represented by (1). The second phase involved the testing of the trained model for the inverse scattering of cylindrical and spherical structures. Results are presented in Section III.B.

This article has been accepted for publication in a future issue of this journal, but has not been fully edited. Content may change prior to final publication. Citation information: DOI 10.1109/OJAP.2021.3057060, IEEE Open Journal of Antennas and Propagation

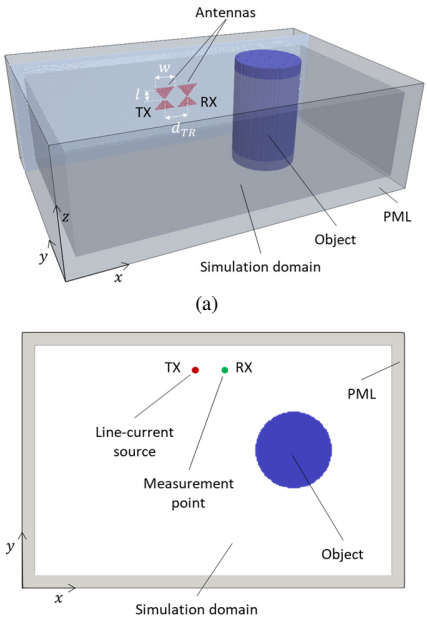

Fig. 4. Configuration of a pair of simulations used for the model training. (a) 3D setup with two bowtie antennas. (b) Corresponding 2D case with line-current source and ideal measurement point.

A. *Forward modeling and network training*

For both simulating the data acquisition and training the proposed LSTM-based network, 3D and 2D EM simulations have been done. As forward solver, the *gprMax* open-source software has been adopted, which allows an efficient FDTD solution of the EM problem with GPU computing capabilities [48].

In each simulated case, a pair of forward simulations have been executed, in order to obtain both $\widetilde{E_{sc}}(\mathbf{r},t)$ and $E_{sc}(\mathbf{r},t)$. The first quantity, which emulates the "actual" measurement, is given by a 3D configuration with two bowtie antennas (a transmitting and a receiving one). The second quantity, which represents the "canonical" measurement situation, is retrieved by simulating a 2D horizontal slice of the previous 3D model, where the transmitting antenna is an infinite z-directed line-current source and the probe is an ideal measurement point (i.e., which does not perturb the EM field).

As to the 3D case, the geometry is reported in Fig. 4(a). The simulation domain has dimensions $L \times W \times D$, with $L = 1.5$ m, $W = 1$ m, $D = 0.5$ m, and is discretized into 6×10^6 cubic FDTD cells of 5 mm side. At the boundaries of the simulation domain, a 10-cells wide perfectly matched layer (PML) has been used to implement absorbing boundary conditions. As a preliminary example, two aligned bowtie antennas are present, at a fixed distance $d_{TR} = 0.12$ m between their centers, each one with arms of width $w = 0.1$ m and height $l = 0.05$ m. The transmitting antenna is driven by a voltage source excited with a Ricker pulse whose spectrum is centered at 1 GHz.

To generate the training data, for each object $V_t = 20$ simulations have been done with different positions of the antennas, where the source element is centered at

$$\mathbf{r}^{TX} = (x_s + L_m(v-1)/(V_t-1)\,, y_s, z_s) \tag{18}$$

and the receiving element is at

$$\mathbf{r}^{RX} = (x_s + L_m(v-1)/(V_t-1) + d_{TR}, y_s, z_s) \tag{19}$$

with $x_s = 0.2$ m, $y_s = 0.85$ m, $z_s = D/2$, $L_m = 1$ m, and $v = 1, \ldots, V_t$. A time window of duration $T = 10$ ns, subdivided into $N = 1040$ samples with a time step $\Delta t = 9.62917$ ps, has been simulated. A dataset composed by 200 different objects has been created, where the simulation domain hosts a single dielectric cylinder (0.5 m high) with random diameter (between 0.2 and 0.6 m), dielectric permittivity (between $1.5\epsilon_0$ and $4\epsilon_0$) and electric conductivity (between 0 S/m and 0.2 S/m). Since each object has been simulated with V_t antenna positions, a global number of 4000 simulations has been run. Among them, the first 3920 were used as the training set, and the last 80 for validation. During the training phase, the minimum distance between the antennas and the targets is equal to 5 cm, leading to near-field operating conditions.

All these 3D simulations have been replicated in the corresponding 2D canonical case, taking into account the cross-sectional slice at $z = z_s$. The geometry is reported in Fig. 4(b) and is analogous to the 3D case, except for the absence of the actual antenna structures. The 2D simulation domain has the same x, y size of the 3D domain ($L \times W$) and the same spatial discretization, resulting in 6×10^4 square FDTD cells. A 10-cells wide PML is adopted. Moreover, a time window T and time step Δt equal to the 3D simulations have been considered. In both 3D and 2D cases, an additional simulation without objects has been done to calculate the scattered field.

The training dataset has been generated on a workstation with an Intel® Core™ i7-2600K CPU at 3.40 GHz, 8 GB of RAM, and an NVIDIA® GeForce® GTX 650 GPU with 1 GB of dedicated RAM. A single 3D simulation required a computational time of 31.6 s, 366 MB of RAM and 544 MB of GPU RAM; 2.9 s, 90.3 MB RAM and 219 MB GPU RAM are needed for running each 2D case.

The LSTM-FC network described in Section II.A has been implemented within a MATLAB environment, which is also used to load the FDTD simulations and perform the training phase. In particular, after heuristic trials, a size of the LSTM cell state $S = 150$ has been chosen, and $H = 40$ neurons have been selected for the two hidden FC layers. The number of real parameters of the LSTM cell is thus equal to $P_{LSTM} = 4(2S + S^2) = 91200$, and the FC layer has $P_{FC} = SH + H^2 + 3H + 1 = 7721$ real coefficients. Therefore, the whole number of parameters to be learned is $P_{LSTM} + P_{FC} = 98921$. The Adam algorithm [49] with mini-batch size of 50 and learning rate 5×10^{-3} has been used to train the network for 20 epochs. For performing the training phase and running the inversion method, a personal computer with an Intel® Core™ i7-5500U CPU at 2.40

This article has been accepted for publication in a future issue of this journal, but has not been fully edited. Content may change prior to final publication. Citation information: DOI 10.1109/OJAP.2021.3057060, IEEE Open Journal of Antennas and Propagation

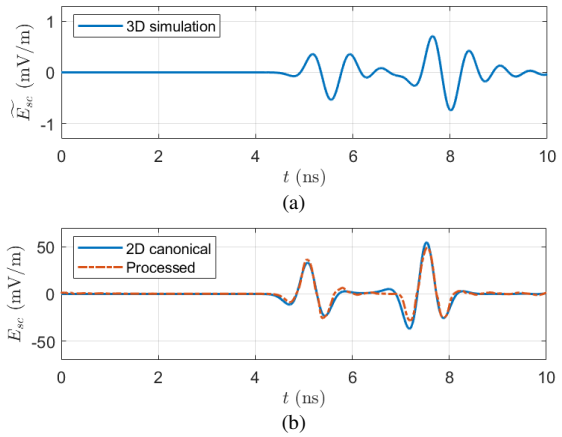

Fig. 5. Example of scattered electric field in the time domain due to a dielectric cylinder. (a) 3D simulation, which represents the input data. (b) Output of the proposed LSTM-based processing block, compared to the corresponding 2D canonical simulation with an ideal measurement setup.

GHz, 8 GB of RAM, and NVIDIA® GeForce® 940M GPU with 2 GB of RAM has been employed. On such a device, the training phase took less than 9 minutes.

An example of the obtained results is shown in Fig. 5, where both $\widetilde{E_{sc}}$ and E_{sc} are reported. In this case (which belongs to the validation set) the object is a circular cylinder with $\epsilon = 2.77\epsilon_0$ and $\sigma = 0.015$ S/m centered at $\mathbf{r}_t = (0.436, 0.325)$ m; the position of antennas is given by (18) and (19) with $v = 12$. The value of $\widetilde{E_{sc}}$ in time domain resulting from the 3D simulation with bowtie antennas is plotted in Fig. 5(a), and its counterpart in the canonical 2D case can be found in Fig. 5(b). In the same figure, the result of applying the proposed LSTM-based preprocessing to $\widetilde{E_{sc}}$ is also shown, which gives rise to a value of E_{sc} quite close to the one obtained in the canonical 2D case with ideal antennas and measurement points.

B. Inverse scattering results

The proposed multifrequency tomographic inversion method enhanced by the data-driven scattered-field processing step has been tested against preliminary numerical simulations. The forward EM simulations have been always performed with the *gprMax* FDTD solver with the same antennas as before, but a slightly different measurement setup is used to collect information all around the object under test. The FDTD simulation domain has side lengths $L \times W \times D$, with $L = W = 1.5$ m, $D = 0.5$ m, and is subdivided into 9×10^6 cubic FDTD cells of 5 mm side. The same time window and temporal discretization have been adopted. A multi-view measurement setup is considered, where the object is sequentially illuminated from $V = 40$ positions of the source antenna, with just one position of the receiving antenna for each view. Despite its simplicity, this kind of measurement configuration is very challenging for the inverse scattering procedure due to the limited available data. In particular, in the vth view ($v = 1, \dots, V$) the position of the source is given by $\mathbf{r}^{TX} = (x^{TX}, y^{TX}, z_s)$ such that

$$x^{TX} = \begin{cases} d_s + \dfrac{L_m(v-1)}{n_s - 1} & 1 \le v \le n_s \\ L - d_t & n_s < v \le 2n_s \\ L - d_s - \dfrac{L_m(v - 2n_s - 1)}{n_s - 1} & 2n_s < v \le 3n_s \\ d_t & 3n_s < v \le V \end{cases} \quad (20)$$

$$y^{TX} = \begin{cases} W - d_t & 1 \le v \le n_s \\ W - d_s - \dfrac{L_m(v - n_s - 1)}{n_s - 1} & n_s < v \le 2n_s \\ d_t & 2n_s < v \le 3n_s \\ d_s + \dfrac{L_m(v - 3n_s - 1)}{n_s - 1} & 3n_s < v \le V \end{cases} \quad (21)$$

where $d_s = 0.2$, $d_t = 0.15$, $n_s = V/4$, and the other parameters are the same as in Section III.A. The receiving element is centered at $\mathbf{r}^{RX} = (x^{RX}, y^{RX}, z_s)$ such that

$$(x^{RX}, y^{RX}) = \begin{cases} (x^{TX} + d_{TR}, y^{TX}) & 1 \le v \le n_s \\ (x^{TX}, y^{TX} - d_{TR}) & n_s < v \le 2n_s \\ (x^{TX} - d_{TR}, y^{TX}) & 2n_s < v \le 3n_s \\ (x^{TX}, y^{TX} + d_{TR}) & 3n_s < v \le V \end{cases} \quad (22)$$

Low-loss objects have been preliminarily considered in this work for validating the proposed approach in the presence of undamped multiple reflections phenomena inside targets, which represents a quite critical situation for the proposed time-domain preprocessing step.

The first considered target is a single circular dielectric cylinder (Cylinder #1) characterized with $\epsilon = 2\epsilon_0$ and $\sigma = 0.01$ S/m, with diameter $d_{c1} = 0.2$ m, centered at the point $\mathbf{r}_t^{c1} = (0.8, 0.55)$ m in the cross-sectional plane. This target configuration is visible in Fig. 6.

The time-domain data corresponding to the scattered electric field $\widetilde{E_{sc}}$ from the 3D simulation with bowtie antennas is reported for all the considered views ($v = 1, \dots, V$) in Fig. 7(a). For comparison purposes, a cross section of the same test case has been simulated also with a 2D canonical setup that involves line-current sources and ideal test points, obtaining the result of Fig. 7(b). The output of the LSTM-FC network, when its input is the scattered field of Fig. 7(a), is reported in Fig. 7(c). It is worth noting that all the views v are separately processed by the neural network in a sequence-to-sequence regression approach. As can be seen, there is a good matching with the canonical 2D data of Fig. 7(b).

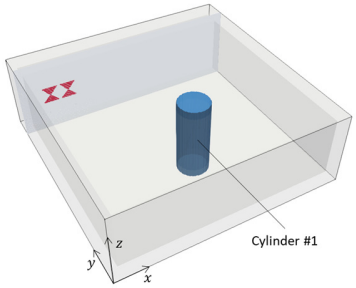

Fig. 6. Configuration of the first target considered for the numerical validation: single dielectric cylinder.

This article has been accepted for publication in a future issue of this journal, but has not been fully edited. Content may change prior to final publication. Citation information: DOI 10.1109/OJAP.2021.3057060, IEEE Open Journal of Antennas and Propagation

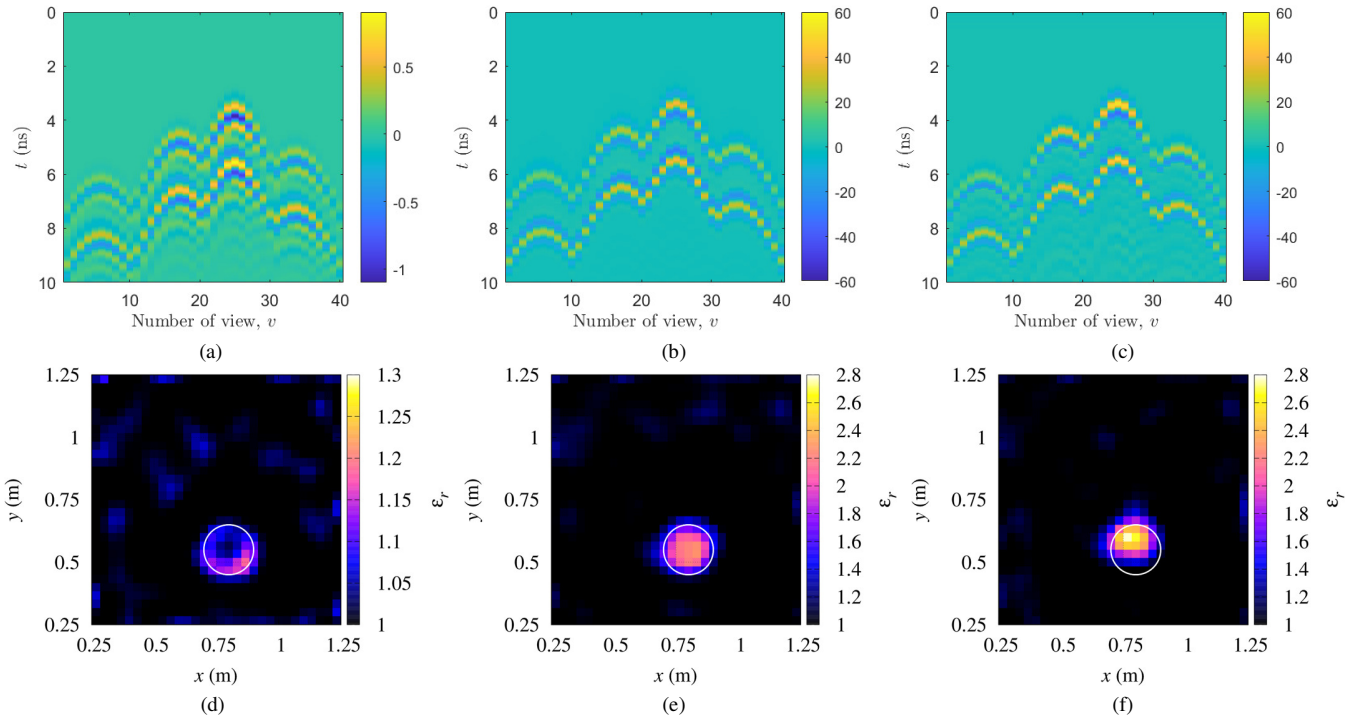

Fig. 7. Numerical results: single dielectric cylinder. Scattered field data in time domain, for different views: (a) 3D simulation; (b) 2D simulation with ideal measurement setup; (c) 3D data processed by the LSTM-based network. Reconstructed distributions of the relative dielectric permittivity with (d) 3D data, (e) 2D data with ideal measurement setup, and (f) 3D data processed by the LSTM-based network.

The next step of the validation consisted in applying the inverse scattering algorithm of Section II.B. To this end, frequency domain data at K frequencies equally spaced between 0.1 and 1 GHz have been extracted with the FFT, obtaining $E_{sc}(\mathbf{r}, f)$ with $\mathbf{r} \in \mathcal{O}$ and $f \in \{f_1, \dots, f_K\}$. It is worth noting that the total electric field in the frequency domain (i.e., after the LSTM-FC processing) has been corrupted with an additive Gaussian noise with zero mean value and $SNR = 25$ dB. The forward solver included in the inversion method is based on a 2D implementation of the method of moments and assumes that line-current sources illuminate the region under test. The investigation domain $\mathcal{I}$ is a square horizontal cross section of the simulated region at the same height of the antenna centers, with dimensions $L_\mathcal{I} = W_\mathcal{I} = 1$ m and centered at point $\mathbf{r} = (0.75 \text{ m}, 0.75 \text{ m}, z_s)$. It has been partitioned into 900 square subdomains with side length 0.033 m. The inversion method has been run with the following parameters: exponent range $\Delta p = 0.5$; maximum numbers of Newton and Landweber iterations equal to 20 and 10, respectively; threshold on the relative variation of the data residual $\Delta r = 1\%$. The reconstructed distributions of the relative permittivity of the investigation domain are reported in Fig. 7(d)-(f). In particular, Fig. 7(d) shows the reconstruction coming from directly using 3D data (with only a simple incident field calibration [35]) which is quite poor and presents a noticeable underestimation of the dielectric properties of the target. Fig. 7(e) shows the reconstruction obtained with the ideal data of Fig. 7(b), i.e., those simulated in 2D settings. Fig. 7(f) illustrates the corresponding reconstruction achieved with the 3D data processed by the LSTM-FC network of Fig. 7(c). In the last two cases, the reconstruction required 114.1 s, and 94.7 s, reporting relative reconstruction errors on the contrast function of 0.13 and 0.14, respectively. The reconstruction obtained with 2D data took slightly more time, mainly due to the different number of performed Newton iterations (5 and 4, respectively), which is related to the stopping criterion based on Δr. As can be seen, the introduction of the LSTM-FC processing enables a quite good retrieval of the dielectric properties of the target, comparable to that yielded by canonical 2D data.

To assess the proposed procedure in a more challenging case, a numerical test with two dielectric cylinders with different properties has been done (Fig. 8). This test is also useful to evaluate the generalization capabilities of the data-driven processing model, since it was trained with configurations including only a single dielectric cylinder.

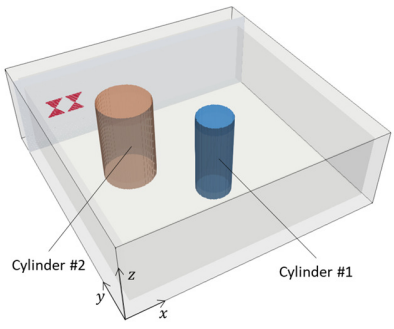

Fig. 8. Configuration of the second target considered for the numerical validation: two dielectric cylinders with different properties.

This article has been accepted for publication in a future issue of this journal, but has not been fully edited. Content may change prior to final publication. Citation information: DOI 10.1109/OJAP.2021.3057060, IEEE Open Journal of Antennas and Propagation

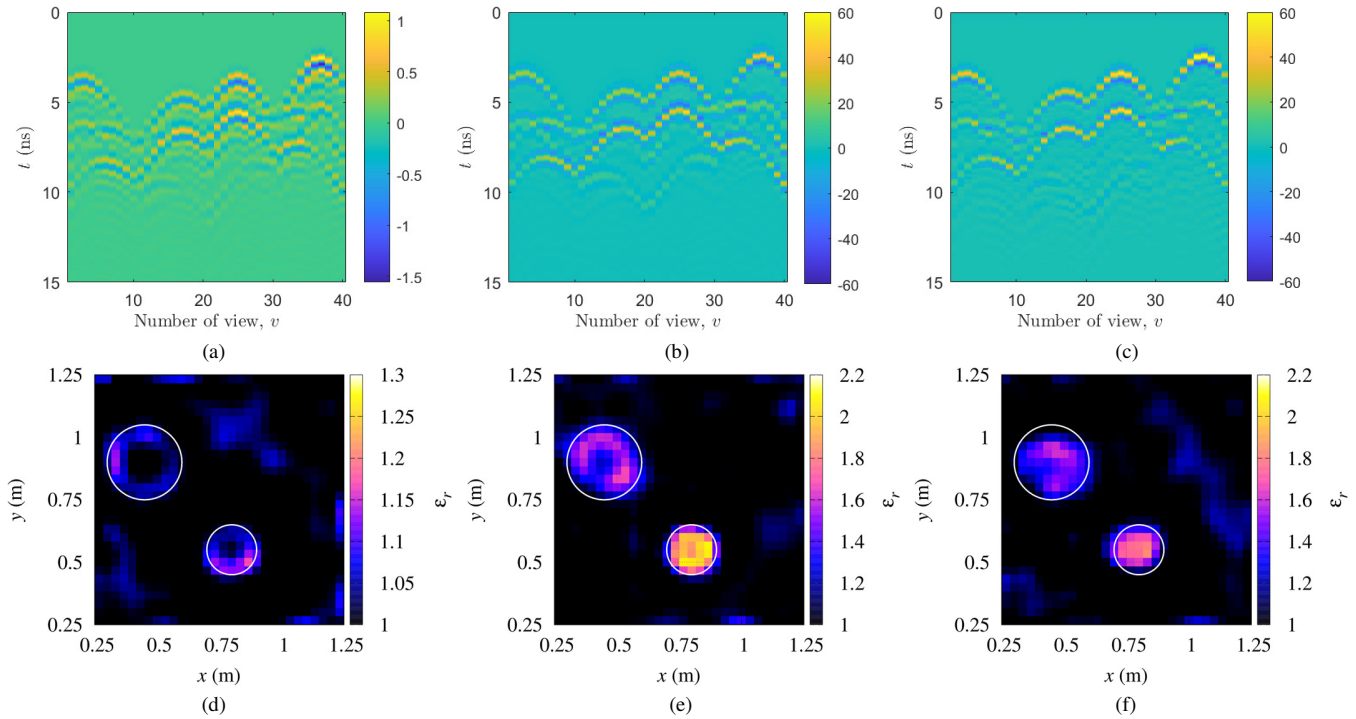

Fig. 9. Numerical results: two dielectric cylinders with different properties. Scattered field data in time domain, for different views: (a) 3D simulation; (b) 2D simulation with ideal measurement setup; (c) 3D data processed by the LSTM-based network. Reconstructed distributions of the relative dielectric permittivity with (d) 3D data, (e) 2D data with ideal measurement setup, and (f) 3D data processed by the LSTM-based network.

In addition to Cylinder #1, a second circular dielectric cylinder (Cylinder #2) characterized with $\epsilon = 1.5\epsilon_0$, $\sigma = 0.005$ S/m and diameter $d_{c2} = 0.3$ m has been placed at $\mathbf{r}_t^{c2} = (0.45, 0.9)$ m in the cross-sectional plane. All the parameters are the same as before except for the simulated time window, which has been enlarged to $T = 15$ ns to allow receiving the multiple reflections between the two targets. It is important to notice that, in general, multiple interactions between targets may be not desirable, especially if linearized scattering models are employed. However, in the present case, to obtain a good quantitative reconstruction it is also required to consider such effects, that arise even in the "ideal" 2D configuration. Therefore, T has been extended to avoid cutting out these phenomena and to see how the proposed LSTM-based network deals with them. This extension has no impact on the network layout, and time sequences of arbitrary lengths can be processed with the same trained model.

Fig. 9(a) and (b) report the scattered field obtained from 3D simulation and from the corresponding 2D simulation with ideal measurement setup. Clearly, reflections from the two different scatterers overlap in time. The 3D data processed by the LSTM-FC network are shown in Fig. 9(c). Although the direct application of the inversion technique to 3D data is again unsatisfactory, as illustrated by Fig. 9(d), the trained network can model the scattered-field data with a reasonable level of accuracy even in this more complicate situation. This is further confirmed by observing the reconstructions of the relative dielectric permittivity reported in Fig. 9(e) and (f). The relative reconstruction errors are 0.15 and 0.16, respectively, with computational times of 83.81 s and 69.20 s (obtained with 4 and 3 Newton iterations). The result achieved starting from the 3D data processed by the LSTM-FC layer is similar to the reconstruction given by the simulation with an ideal measurement setup, except a slight underestimation of the target properties and some background artefacts. These small differences are however tolerable in the light of the significant advantages of avoiding a cumbersome EM modeling inside the inversion algorithm. It is important to remark that, in these cases, the minimum distances between antennas and targets are equal to 30 cm (Cylinder #1) and 15 cm (Cylinder #2). Considering the frequency band adopted for the reconstructions, these distances correspond to near-field conditions, i.e., a situation where a strong coupling between targets and antennas occurs.

In order to further test the capabilities of the developed LSTM-FC preprocessing approach, two more complex target configurations have been simulated, both of them including objects significantly different from those of the training set.

The first case involves a dielectric sphere [Sphere #1, shown in Fig. 10(a)] which is characterized by diameter $d_{s1} = 0.3$ m, dielectric permittivity $\epsilon = 2\epsilon_0$ and electric conductivity $\sigma = 0.01$ S/m. The target is centered at $\mathbf{r}^{s1} = (0.6, 0.9, z_s)$ m. All simulation and inversion parameters are kept the same as before. The reconstruction obtained by directly using 3D data is reported in Fig. 10(b), whereas the

This article has been accepted for publication in a future issue of this journal, but has not been fully edited. Content may change prior to final publication. Citation information: DOI 10.1109/OJAP.2021.3057060, IEEE Open Journal of Antennas and Propagation

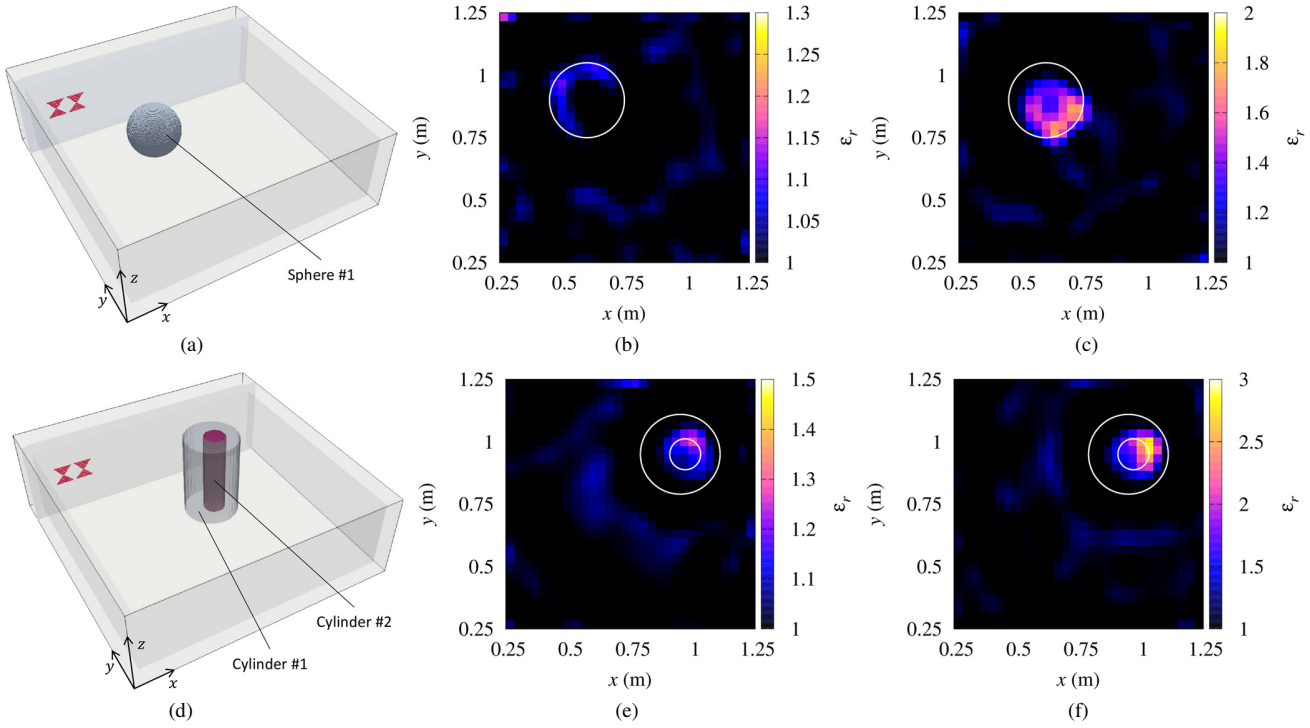

Fig. 10. Numerical results. Dielectric sphere: (a) Target configuration; Reconstructed relative dielectric permittivity with (b) unprocessed 3D data; (c) 3D data processed by the LSTM-based network. Inhomogeneous dielectric target: (d) Configuration; Reconstructed relative dielectric permittivity with (e) unprocessed 3D data; (f) 3D data processed by the LSTM-based network.

processed data give rise to the result of Fig. 10(c). Although the considered target is intrinsically three-dimensional, the developed processing method leads to an acceptable dielectric reconstruction, with a notable improvement compared to the unprocessed data (in terms of both localization and characterization accuracy).

Finally, an inhomogeneous target has been taken into account [Fig. 10(d)]. This target, whose cross section has been inspired by the well-known Fresnel dataset [50], is composed by two nested circular dielectric cylinders. Cylinder #1 is characterized by $\epsilon = 1.3\epsilon_0$, $\sigma = 0.01$ S/m, diameter $d_{c1} = 0.32$ m and is centered at the point $\mathbf{r}_t^{c1} = (0.95, 0.95)$ m. Cylinder #2 is placed inside Cylinder #1; it has diameter $d_{c2} = 0.124$ m, center $\mathbf{r}_t^{c2} = (0.97, 0.95)$ m and is characterized by $\epsilon = 5\epsilon_0$, $\sigma = 0.005$ S/m. The reason for choosing such values of the dielectric permittivity was also to test the method with an object characterized by values of permittivity outside the range of the training set. The dielectric reconstruction obtained with unprocessed 3D data is reported in Fig. 10(e), while Fig. 10(f) shows the results achieved by applying the inversion algorithm to the 3D data processed by the proposed network. The target appears slightly shifted, and the reconstruction is less accurate than before. Furthermore, the retrieved values of the permittivity are "compressed" in the range of those considered inside the training set. (This fact also happens by changing the dielectric properties of the targets in Fig. 8; results are not shown for brevity.) However, despite the inaccuracies caused by the more involving configuration, the enhancement given by the LSTM-FC processing network is still relevant. Since the proposed method is data-driven, further improvements are expected if the training set is enriched by additional inhomogeneous targets, as well as involving wide ranges of their dielectric properties.

IV. Conclusion

In the field of microwave tomography, an adequate modeling of the measured scattered-field data is crucial to retrieve correct quantitative reconstructions of the properties of unknown scatterers. In this contribution, the combination of a data-driven LSTM-based preprocessing of the scattered field with a nonlinear multifrequency tomographic approach in Lebesgue spaces with nonconstant exponents has been investigated. The proposed strategy enables quite accurate inversion results starting from simulated measurements in 3D cylindrical settings with non-ideal probes, while retaining a 2D canonical formulation of the electromagnetic problem inside the imaging algorithm. The data-driven preprocessing network has been trained with time-domain numerical simulations involving cylindrical targets, where a simplified bistatic measurement configuration has been taken as a preliminary case study. The inversion procedure has been assessed in a simulated environment.

Future developments of this study will include the extension of the proposed approach to more involved measurement configurations (e.g., the multistatic case) as well as the testing with lossy targets and experimental data.

This article has been accepted for publication in a future issue of this journal, but has not been fully edited. Content may change prior to final publication. Citation information: DOI 10.1109/OJAP.2021.3057060, IEEE Open Journal of Antennas and Propagation

The possible extension to the frequency domain of concepts derived from the present approach will also be analyzed. In addition, since CNNs and LSTMs are not mutually exclusive, the use of CNN-LSTM hybrid networks to accomplish this task will be explored.

ACKNOWLEDGMENT

The Author would like to acknowledge the support of the Applied Electromagnetics Group at the University of Genoa, Italy, for the development of the inverse scattering procedure.

REFERENCES

[1] J.-C. Bolomey, "Advancing Microwave-Based Imaging Techniques for Medical Applications in the Wake of the 5G Revolution," in *Proceedings of the 13th European Conference on Antennas and Propagation*, Krakow, Poland, 2019, pp. 1–5.

[2] O. M. Bucci, G. Bellizzi, S. Costanzo, L. Crocco, G. Di Massa, and R. Scapaticci, "Assessing detection limits in magnetic nanoparticle enhanced microwave imaging," *IEEE Access*, vol. 6, pp. 43192–43202, 2018.

[3] Q. Guo, Y. Li, X. Liang, J. Dong, and R. Cheng, "Through-the-Wall Image Reconstruction via Reweighted Total Variation and Prior Information in Radio Tomographic Imaging," *IEEE Access*, vol. 8, pp. 40057–40066, 2020.

[4] A. Fedeli, M. Pastorino, C. Ponti, A. Randazzo, and G. Schettini, "Through-the-Wall Microwave Imaging: Forward and Inverse Scattering Modeling," *Sensors*, vol. 20, no. 10, p. 2865, Jan. 2020.

[5] I. Catapano, A. Randazzo, E. Slob, and R. Solimene, "GPR imaging via qualitative and quantitative approaches," in *Civil Engineering Applications of Ground Penetrating Radar*, A. Benedetto and L. Pajewski, Eds. Cham: Springer International Publishing, 2015, pp. 239–280.

[6] N. K. Nikolova, *Introduction to Microwave Imaging*. Cambridge: Cambridge University Press, 2017.

[7] M. Pastorino and A. Randazzo, *Microwave Imaging Methods and Applications*. Boston, MA: Artech House, 2018.

[8] A. Dell'Aversano, G. Leone, F. Ciaramaglia, and R. Solimene, "A strategy for reconstructing simple shapes from undersampled backscattered data," *IEEE Geoscience and Remote Sensing Letters*, vol. 13, no. 12, pp. 1757–1761, 2016.

[9] R. Scapaticci, J. Tobon, G. Bellizzi, F. Vipiana, and L. Crocco, "Design and numerical characterization of a low-complexity microwave device for brain stroke monitoring," *IEEE Transactions on Antennas and Propagation*, vol. 66, no. 12, pp. 7328–7338, Dec. 2018.

[10] V. L. Coli, P.-H. Tournier, V. Dolean, I. E. Kanfoud, C. Pichot, C. Migliaccio, *et al.*, "Detection of simulated brain strokes using microwave tomography," *IEEE Journal of Electromagnetics, RF and Microwaves in Medicine and Biology*, vol. 3, no. 4, pp. 254–260, Dec. 2019.

[11] M. T. Bevacqua, T. Isernia, R. Palmeri, M. N. Akinci, and L. Crocco, "Physical insight unveils new imaging capabilities of orthogonality sampling method," *IEEE Transactions on Antennas and Propagation*, vol. 68, no. 5, pp. 4014–4021, May 2020.

[12] S. C. Pavone, G. Sorbello, and L. Di Donato, "On the Orbital Angular Momentum Incident Fields in Linearized Microwave Imaging," *Sensors*, vol. 20, no. 7, p. 1905, Jan. 2020.

[13] N. Bayat and P. Mojabi, "On the Use of Focused Incident Near-Field Beams in Microwave Imaging," *Sensors*, vol. 18, no. 9, p. 3127, Sep. 2018.

[14] M. Ettorre, S. C. Pavone, M. Casaletti, M. Albani, A. Mazzinghi, and A. Freni, "Near-Field Focusing by Non-diffracting Bessel Beams," in *Aperture Antennas for Millimeter and Sub-Millimeter Wave Applications*, A. Boriskin and R. Sauleau, Eds. Cham: Springer International Publishing, 2018, pp. 243–288.

[15] D. Comite, W. Fuscaldo, S. C. Pavone, G. Valerio, M. Ettorre, M. Albani, *et al.*, "Propagation of nondiffracting pulses carrying orbital angular momentum at microwave frequencies," *Appl. Phys. Lett.*, vol. 110, no. 11, p. 114102, Mar. 2017.

[16] C. Ponti, P. Baccarelli, S. Ceccuzzi, and G. Schettini, "Tapered All-Dielectric EBGs with 3D Additive Manufacturing for High-Gain Resonant-Cavity Antennas," *IEEE Transactions on Antennas and Propagation*, pp. 1–1, 2020.

[17] S. Poretti, M. Lanini, A. Salvadè, M. Maffongelli, and R. Monleone, "Antenna design for microwave tomography imaging of high contrast mediums," in *Proceedings of the 11th European Conference on Antennas and Propagation*, Paris, France, 2017, pp. 1699–1702.

[18] A. Salvade, M. Pastorino, R. Monleone, G. Bozza, and A. Randazzo, "A new microwave axial tomograph for the inspection of dielectric materials," *IEEE Transactions on Instrumentation and Measurement*, vol. 58, no. 7, pp. 2072–2079, Jul. 2009.

[19] A. Fedeli, M. Maffongelli, R. Monleone, C. Pagnamenta, M. Pastorino, S. Poretti, *et al.*, "A tomograph prototype for quantitative microwave imaging: preliminary experimental results," *Journal of Imaging*, vol. 4, no. 12, p. 139, Dec. 2018.

[20] A. H. Golnabi, P. M. Meaney, S. D. Geimer, and K. D. Paulsen, "3-D Microwave Tomography Using the Soft Prior Regularization Technique: Evaluation in Anatomically Realistic MRI-Derived Numerical Breast Phantoms," *IEEE Transactions on Biomedical Engineering*, vol. 66, no. 9, pp. 2566–2575, Sep. 2019.

[21] S. D. Campbell, R. P. Jenkins, P. J. O'Connor, and D. Werner, "The Explosion of Artificial Intelligence in Antennas and Propagation: How Deep Learning is Advancing Our State of the Art," *IEEE Antennas and Propagation Magazine*, in press.

[22] A. Massa, D. Marcantonio, X. Chen, M. Li, and M. Salucci, "DNNs as Applied to Electromagnetics, Antennas, and Propagation—A Review," *IEEE Antennas and Wireless Propagation Letters*, vol. 18, no. 11, pp. 2225–2229, Nov. 2019.

[23] X. Chen, Z. Wei, M. Li, and P. Rocca, "A review of deep learning approaches for inverse scattering problems," *Progress In Electromagnetics Research*, vol. 167, pp. 67–81, 2020.

[24] K. Edwards, N. Geddert, K. Krakalovich, R. Kruk, M. Asefi, J. Lovetri, *et al.*, "Stored Grain Inventory Management Using Neural-Network-Based Parametric Electromagnetic Inversion," *IEEE Access*, vol. 8, pp. 207182–207192, 2020.

[25] Y. Sanghvi, Y. Kalepu, and U. K. Khankhoje, "Embedding Deep Learning in Inverse Scattering Problems," *IEEE Transactions on Computational Imaging*, vol. 6, pp. 46–56, 2020.

[26] Z. Wei and X. Chen, "Physics-inspired convolutional neural network for solving full-wave inverse scattering problems," *IEEE Transactions on Antennas and Propagation*, vol. 67, no. 9, pp. 6138–6148, Sep. 2019.

[27] L. Li, L. G. Wang, F. L. Teixeira, C. Liu, A. Nehorai, and T. J. Cui, "DeepNIS: Deep neural network for nonlinear electromagnetic inverse scattering," *IEEE Trans. Antennas Propagat.*, vol. 67, no. 3, pp. 1819–1825, Mar. 2019.

[28] A. Abubakar, T. M. Habashy, V. L. Druskin, and L. Knizhnerman, "An enhanced Gauss-Newton inversion algorithm using a dual-optimal grid approach," *IEEE Transactions on Geoscience and Remote Sensing*, vol. 44, no. 6, pp. 1419–1427, Jun. 2006.

[29] P. Mojabi and J. LoVetri, "A prescaled multiplicative regularized Gauss-Newton inversion," *IEEE Transactions on Antennas and Propagation*, vol. 59, no. 8, pp. 2954–2963, Aug. 2011.

[30] M. Ostadrahimi, P. Mojabi, A. Zakaria, J. LoVetri, and L. Shafai, "Enhancement of Gauss-Newton inversion method for biological tissue imaging," *IEEE Transactions on Microwave Theory and Techniques*, vol. 61, no. 9, pp. 3424–3434, Sep. 2013.

[31] C. Estatico, A. Fedeli, M. Pastorino, and A. Randazzo, "Microwave imaging by means of Lebesgue-space inversion: An overview," *Electronics*, vol. 8, no. 9, p. 945, Sep. 2019.

[32] I. Bisio, C. Estatico, A. Fedeli, F. Lavagetto, M. Pastorino, A. Randazzo, *et al.*, "Variable-exponent Lebesgue-space inversion for brain stroke microwave imaging," *IEEE Transactions on Microwave Theory and Techniques*, vol. 68, no. 5, pp. 1882–1895, May 2020.

[33] C. Estatico, A. Fedeli, M. Pastorino, A. Randazzo, and E. Tavanti, "A phaseless microwave imaging approach based on a Lebesgue-space inversion algorithm," *IEEE Transactions on Antennas and Propagation*, vol. 68, no. 12, pp. 8091–8103, Dec. 2020.

[34] A. Fedeli, V. Schenone, A. Randazzo, M. Pastorino, T. Henriksson, and S. Semenov, "Nonlinear S-parameters inversion for stroke imaging," *IEEE Transactions on Microwave Theory and Techniques*, in press.

This article has been accepted for publication in a future issue of this journal, but has not been fully edited. Content may change prior to final publication. Citation information: DOI 10.1109/OJAP.2021.3057060, IEEE Open Journal of Antennas and Propagation

[35] M. Ostadrahimi, P. Mojabi, C. Gilmore, A. Zakaria, S. Noghanian, S. Pistorius, *et al.*, "Analysis of incident field modeling and incident/scattered field calibration techniques in microwave tomography," *IEEE Antennas and Wireless Propagation Letters*, vol. 10, pp. 900–903, 2011.

[36] A. Litman, J.-M. Geffrin, and and H. Tortel, "On the Calibration of a Multistatic Scattering Matrix Measured by a Fixed Circular Array of Antennas," *Progress In Electromagnetics Research*, vol. 110, pp. 1–21, 2010.

[37] P. Mojabi, M. Ostadrahimi, L. Shafai, and J. LoVetri, "Microwave tomography techniques and algorithms: A review," in *2012 15 International Symposium on Antenna Technology and Applied Electromagnetics*, 2012, pp. 1–4.

[38] G. Govind and M. J. Akhtar, "Microwave Nondestructive Imaging of Buried Objects Using Improved Scattered-Field Calibration Technique," *Radio Science*, vol. 53, no. 1, pp. 2–14, 2018.

[39] S. Lambot, E. C. Slob, I. van den Bosch, B. Stockbroeckx, and M. Vanclooster, "Modeling of ground-penetrating radar for accurate characterization of subsurface electric properties," *IEEE Transactions on Geoscience and Remote Sensing*, vol. 42, no. 11, pp. 2555–2568, Nov. 2004.

[40] S. Lambot and F. André, "Full-wave modeling of near-field radar data for planar layered media reconstruction," *IEEE Transactions on Geoscience and Remote Sensing*, vol. 52, no. 5, pp. 2295–2303, May 2014.

[41] J. W. Zhang, S. B. Ye, H. Liu, L. Yi, and G. Y. Fang, "Filtering out Antenna Effects From GPR Data by an RBF Neural Network," *IEEE Geoscience and Remote Sensing Letters*, vol. 16, no. 9, pp. 1378–1382, Sep. 2019.

[42] S. Hochreiter and J. Schmidhuber, "Long Short-Term Memory," *Neural Computation*, vol. 9, no. 8, pp. 1735–1780, Nov. 1997.

[43] R. Pascanu, T. Mikolov, and Y. Bengio, "On the difficulty of training Recurrent Neural Networks," in *arXiv:1211.5063 [cs]*, Atlanta, Georgia, USA, 2013.

[44] K. Greff, R. K. Srivastava, J. Koutník, B. R. Steunebrink, and J. Schmidhuber, "LSTM: A Search Space Odyssey," *IEEE Transactions on Neural Networks and Learning Systems*, vol. 28, no. 10, pp. 2222–2232, Oct. 2017.

[45] O. Noakoasteen, S. Wang, Z. Peng, and C. Christodoulou, "Physics-Informed Deep Neural Networks for Transient Electromagnetic Analysis," *IEEE Open Journal of Antennas and Propagation*, vol. 1, pp. 404–412, 2020.

[46] W. Lei, J. Luo, F. Hou, L. Xu, R. Wang, and X. Jiang, "Underground Cylindrical Objects Detection and Diameter Identification in GPR B-Scans via the CNN-LSTM Framework," *Electronics*, vol. 9, no. 11, p. 1804, Nov. 2020.

[47] C. Estatico, A. Fedeli, M. Pastorino, and A. Randazzo, "Quantitative microwave imaging method in Lebesgue spaces with nonconstant exponents," *IEEE Transactions on Antennas and Propagation*, vol. 66, no. 12, pp. 7282–7294, Dec. 2018.

[48] C. Warren, A. Giannopoulos, and I. Giannakis, "gprMax: Open source software to simulate electromagnetic wave propagation for Ground Penetrating Radar," *Computer Physics Communications*, vol. 209, pp. 163–170, Dec. 2016.

[49] D. P. Kingma and J. Ba, "Adam: A Method for Stochastic Optimization," *arXiv:1412.6980 [cs]*, Jan. 2017.

[50] J.-M. Geffrin, P. Sabouroux, and C. Eyraud, "Free space experimental scattering database continuation: experimental set-up and measurement precision," *Inverse Problems*, vol. 21, no. 6, pp. S117–S130, Dec. 2005.

Alessandro Fedeli (S'14–M'17) received the B.Sc. and M.Sc. degrees in electronic engineering and the Ph.D. degree in science and technology for electronic and telecommunications engineering from the University of Genoa, Genoa, Italy, in 2011, 2013, and 2017, respectively. He is currently an Assistant Professor at the Department of Electrical, Electronic, Telecommunications Engineering, and Naval Architecture, University of Genoa. His research activities, carried out at the Applied Electromagnetics Laboratory, are mainly focused on the development and the application of computational methods for the solution of forward and inverse scattering problems, and electromagnetic imaging. He has coauthored more than 100 scientific contributions published in international journals and conference proceedings. Dr. Fedeli is member of the IEEE Antennas and Propagation Society, the Italian Society of Electromagnetism, and the Interuniversity Center for the Interaction between Electromagnetic Fields and Biosystems.